Characterization of Non-Metallic Inclusions in Superelastic NiTi Tubes

Alejandro Toro, Fei Zhou, Ming H. Wu, William Van Geertruyden, and Wojciech Z. Misiolek

Non-metallic inclusions have been shown frequently to lead to crack initiation in superelastic Nitinol fatigue specimens. While prior studies suggested that both carbide (TiC) and oxide (Ti$_4$Ni$_2$O$_x$) inclusions can develop in superelastic Nitinol alloys, questions remain on whether or how the chemistry and morphology of these non-metallic inclusions are affected by the melting and subsequent tube manufacturing process. In the present study, samples of Ti-55.8wt.%Ni alloy were taken from tubes fabricated from materials of various VIM and VAR melt processes. Additional samples were taken from various stages of the tube drawing process for studying the stringer formation. Our results suggest that both carbide and oxide inclusions are present in VIM/VAR materials and the oxide break-down during tube drawing appears to be the primary mechanism for stringer formation. Carbides in VIM materials generally remain as isolated particles during tube fabrication while the primary inclusion of oxide in the VAR material explains its higher stringer density. In addition, the carbide inclusion has been confirmed to contain a noticeable amount of oxygen; hence, we suggest the "Ti(C, O)" nomenclature. Further study on the role of oxygen on carbide and oxide formation in VIM/VAR materials may be beneficial for improving the future melt quality of NiTi alloys.

1. Introduction

Superelasticity is a key characteristic for selecting NiTi alloys for medical implant devices because it offers the possibility of designing a self-expanding device with a small delivery profile and compliance similar to that of the natural anatomy. For example, treating diseases such as stenosis in superficial femoral, iliac and popliteal arteries where the devices are subjected to complex deformations, self-expanding NiTi stents have been proven to perform better than do stainless steel stents in clinical outcomes owing to the more compliant mechanical properties and reduced thrombogenicity (Ref 1). However, these difficult anatomies inevitably impose severe dynamic deformations on the material, which can lead to device fracture and negative clinical outcomes (Ref 2). Hence, fatigue lifetime is a critical consideration for device durability in self-expanding NiTi implant designs.

Alejandro Toro, National University of Colombia, Medellin, Colombia; **Fei Zhou** and **Ming H. Wu**, Edwards LifeSciences LLC, Irvine, CA; **William Van Geertruyden**, EMV Technologies, LLC, Bethlehem, PA; and **Wojciech Z. Misiolek**, Institute for Metal Forming, Lehigh University, Bethlehem, PA. Contact e-mail: Ming_Wu@Edwards.com.

Fatigue fractures in NiTi test specimens have often been observed to initiate from non-metallic inclusions (Ref 3, 4). It is well known in the metal industry that non-metallic inclusions are influenced primarily by the melting technique. At the present time, commercial NiTi alloys are produced by vacuum induction melting (VIM), vacuum arc melting (VAR), or a hybrid process where the primary VIM ingot is further refined using a VAR process (VIM/VAR) (Ref 5). Because the VIM process uses graphite crucibles, carbon pickup during melting leads to a greater level of carbon impurity of 300-700 ppm in VIM ingots as compared to less than 100 ppm in VAR ingots (Ref 5). Reinoehl et al. (Ref 3) studied the effects of carbon content on inclusions and rotating-beam fatigue of re-draw wires of significantly different carbon contents from two different suppliers. They reported that the material of lower carbon content had less inclusion count but the inclusion size was much larger than those of material having higher carbon content. The authors however did not observe any significant difference in the fatigue lifetimes between the two materials.

It has been recognized that both TiC and Ti$_4$Ni$_2$O$_x$ non-metallic inclusions can develop in NiTi alloys (Ref 6). Studying the inclusions in Ti-50.7at.%Ni alloys prepared by a laboratory scale VIM furnace using a graphite crucible, Zhang et al. (Ref 7) detected eutectic TiC in an as-cast ingot with 200 ppm carbon. But for ingot having 710 ppm carbon, both eutectic TiC and primary TiC were present in the as-cast structure. Habu et al. (Ref 4) in their study on VIM alloys observed only TiC in the as-cast ingot. While TiC remained present at various stages of the tube manufacturing process, Ti$_4$Ni$_2$O$_x$ was occasionally detected in finished tubes.

Graham et al. (Ref 8) studied the inclusions in VAR Ti-50.8at.%Ni alloys in details. By controlling the melt process and input stocks, the authors produced sample ingots of 250-280 ppm oxygen and less than 30 ppm carbon as well as an

ultra-clean variant with oxygen and carbon contents of less than 50 and 20 ppm, respectively. The non-metallic chemistry was not analyzed but assumed to be $Ti_4Ni_2O_x$. The study demonstrated that the ingot size, and hence the solidification rate, can influence the inclusion size. In the ultra-clean variant, both the area fraction and size of inclusion were significantly reduced. However, they reported inferior fatigue lifetimes of ultra-clean material when compared to those of the typical VAR melt variants attributing the anomaly to the dominant influence of surface finish. A further study by Morgan et al. (Ref 9) suggested that ultra-low carbon and oxygen impurity levels do improve melt cleanliness and reduce inclusion. Fatigue study of electro-polished wires demonstrated slightly improved fatigue lifetimes in the long life regime with the low inclusion material compared with those of standard VAR and VIM/VAR materials.

In our experience of fatigue testing superelastic NiTi tube specimens, we have encountered significant variations in inclusion morphology and fatigue durability of materials processed using various melt processes. These inconsistencies were observed even in materials fabricated by the same melt technique. It is therefore not our intent to compare the fatigue durability of materials prepared by various melting techniques based on limited sample population. However, quite often crack initiation in prematurely failed specimens can be linked to stringers, an elongated cluster of fractured inclusions as shown in Fig. 1(a) while crack initiation in specimens failing at "normal" durability cycles is more typically linked to a small isolated inclusion particle; an example is shown in Fig. 1(b). As we continue to develop knowledge of the prejudicial effect of non-metallic inclusions on the fatigue resistance of Ni-Ti

alloys, it is reasonable to anticipate some correlations that must exist among their chemical composition, size, shape, and distribution in the microstructure. Many of these factors are influenced by not only the melting technique but also the subsequent thermal and mechanical conversion process for making semi-finished products such as wires and tubes. In the present study, chemistries of non-metallic inclusions in commercial Ti-50.8at.%Ni alloys manufactured by VIM, VIM/VAR, and VAR processes were analyzed using various techniques of electron microscopy. The inclusion morphologies at various stages of the tube fabrication process of a VIM/VAR alloy were examined in detail. The aim is to provide further understanding on the effect of melting process on inclusion chemistry as well as those on stringer formation during the subsequent tube manufacturing process.

2. Experimental Procedure

Tubes of 2.2 mm outside diameter fabricated from materials of VIM/VAR, VIM, and VAR melt processes were used in the present study. Samples of a VIM/VAR alloy taken at different stages of the tube drawing process were also analyzed. The specimen identifications and related material information are tabulated in Table 1.

All the samples were prepared according to standard metallographic specimen preparation procedure and finished by automatic vibratory polishing in cloth with 0.05 μm SiO_2 particles. Specimens for optical microscopy were examined in

Table 1 Description of specimens used in the study

ID#	Melt process	Ingot Ap temperature, °C	Carbon, ppm	Oxygen, ppm	Tube fabrication stage
A1	VIM/VAR	−8	324	262	Hot rolled bar 31.0 mm OD
A2	VIM/VAR	−8	324	262	Intermediate 6.7 mm OD
A3	VIM/VAR	−8	324	262	Finished tube 2.2 mm OD
B	VIM	+4	240	300	Finished tube 2.2 mm OD
C	Standard VAR	+4	34	310	Finished tube 2.2 mm OD
D	HP VAR	−19	<20	<50	Finished tube 2.2 mm OD

OD, outside diameter; HP, high purity

(a)　　　　**(b)**
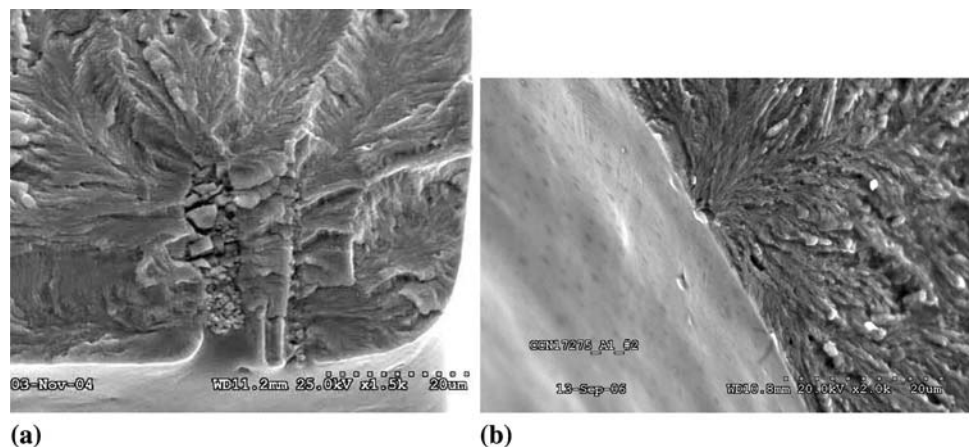
Fig. 1 SEM micrographs of fatigue fractured surface showing the crack initiation site of (a) a stringer of inclusions in a prematurely failed specimen and (b) an isolated inclusion particle in a specimen failed at a typical durability cycle
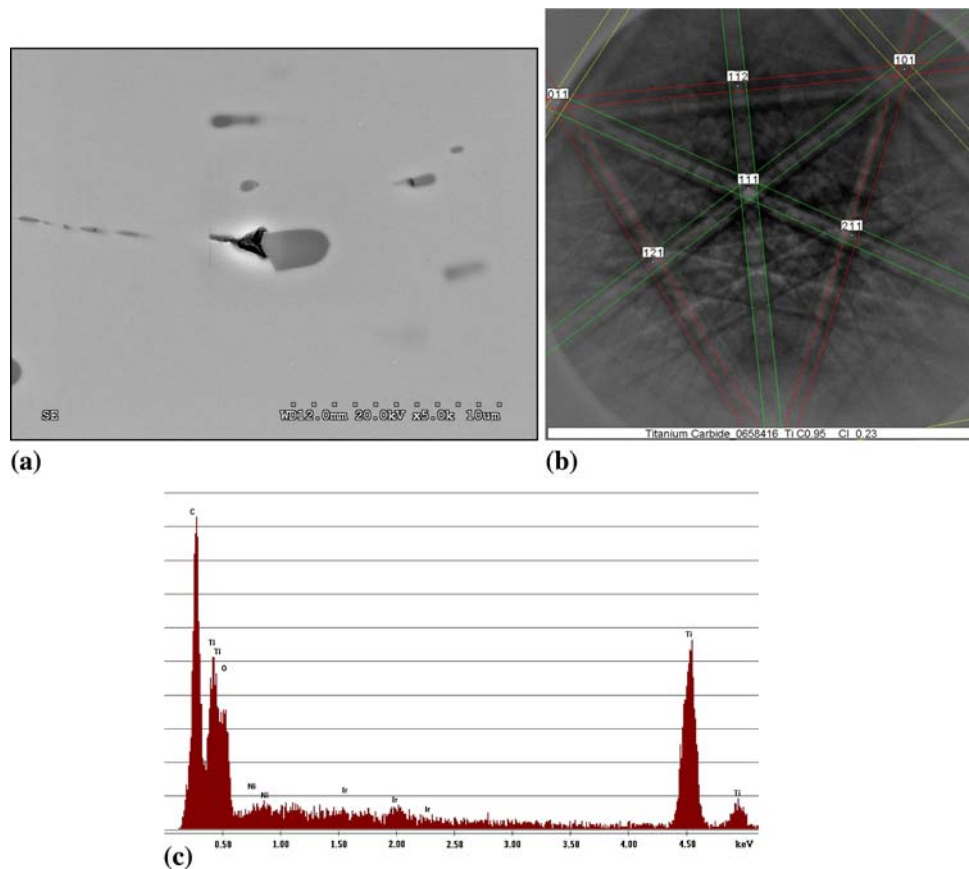
Fig. 2 (a) Secondary electron SEM image of a typical carbide in specimen A1, (b) corresponding indexed EBSD pattern, and (c) EDS spectrum which determined the most likely phase to be Ti(C, O) carbide

lightly etched condition. Etchant of $HF/HNO_3/H_2O$, 3:10:87 in volumetric ratio, was used to bring up the inclusion contrast. Preferential etching was found to often remove certain inclusions from the surface. Therefore, for the SEM study, all samples were polished and coated with a thin layer of amorphous Ir by using a sputtering current of 20 nA and sputtering time of 3 s. The analyses were made using an Olympus BH2 light optical microscope (LOM), a Hitachi 4300 field emission gun scanning electron microscope (FEG-SEM) in conjunction with TSL/EDAX electron backscatter diffraction (EBSD) and energy dispersive spectroscopy (EDS) systems, and Auger electron spectroscopy (AES) using a PHI Smart-200 FE-Nanoprobe instrument. An acceleration voltage of 10 kV was used for all the EDS measurements to improve spatial resolution, while 20 kV were applied for all the EBSD and AES measurements. The AES specimen was sputter-cleaned using Ar^+ ion prior to the analysis.

3. Results and Discussion

3.1 Basic Identification of Inclusions' Type

3.1.1 Carbide-Type Inclusions. Figure 2(a) shows a secondary electron image of a carbide inclusion in the A1 specimen. Some plastic flow of the matrix around these particles was observed, namely the "tail" to the left of the inclusion. The EBSD pattern obtained closely matches the cubic structure of TiC (Fig. 2b) and the EDS spectra shows mostly C, O, and Ti peaks with only a trace amount of Ni (Fig. 2c). Figure 3(a) shows an SEM micrograph of both carbide and oxide inclusions in specimen A3. The carbide appears darker than oxide due to the Z-contrast of lighter elements in the composition. The EDS line scan of Fig. 3(b) indicates that the carbide is more enriched in Ti, C, and O, and depleted in Ni than the matrix.

The reason for using the "Ti(C, O)" nomenclature is that after a significant number of EDS and line scan analyses some amount of O was consistently detected together with Ti and C. The presence of O in carbide was further confirmed by AES; a typical spectrum of the carbide inclusion shown in Fig. 4(b) undoubtedly demonstrates the presence of O in Auger electron signal. Since the crystal structures of both TiC and TiO are cubic and the mean difference between their lattice parameters is only 6% (Ref 10), these results may indicate that part of the C atoms in the TiC structure could have been replaced by O atoms, configuring a substitutional crystal. It is worth noticing that these particles are not complex oxide-carbide compounds, given that their structure is always cubic and compatible with that of TiC.

3.1.2 Oxide-Type Inclusions. Analyses of an oxide inclusion in specimen A1 are shown in Fig. 5. These particles are, in general, larger than the carbides and their shape is more irregular (Fig. 5a). The EBSD patterns closely matched the cubic structure of the $Ti_4Ni_2O_x$ (Fig. 5b) (Ref 10) and the EDS spectra revealed the presence of less Ti and C, about the same amount of O but much higher Ni content (Fig. 5c) than in the
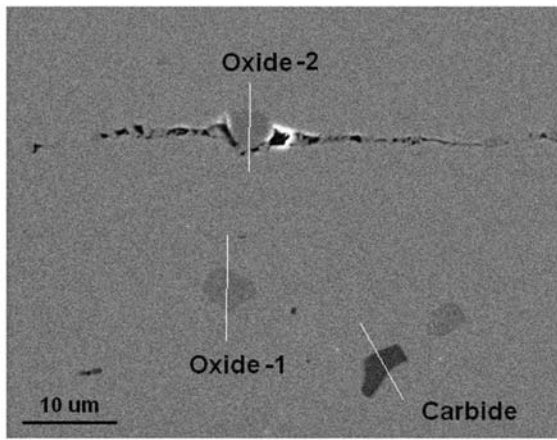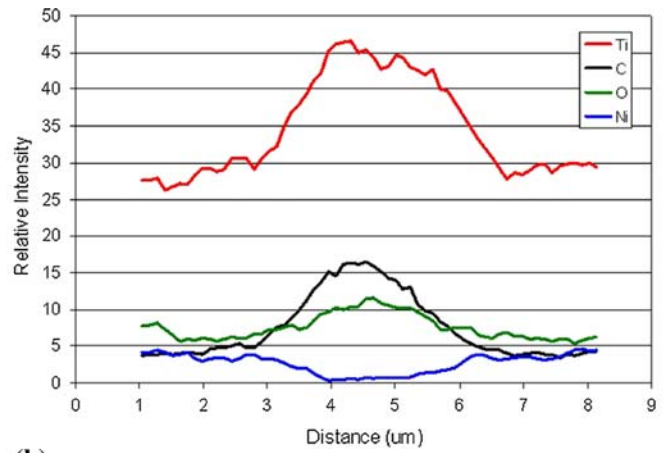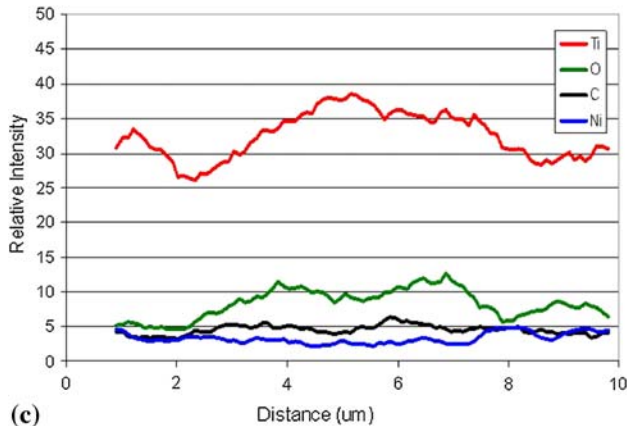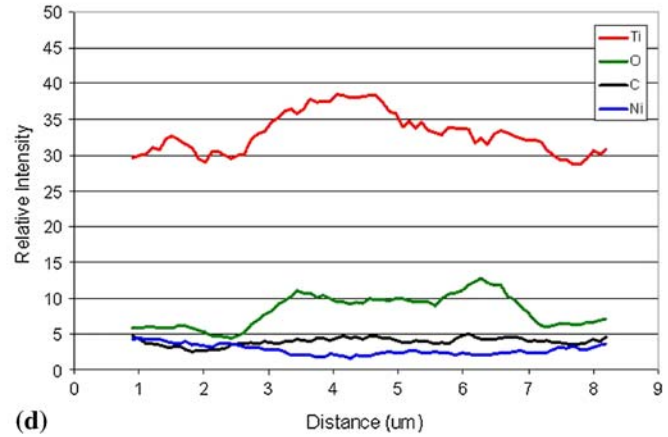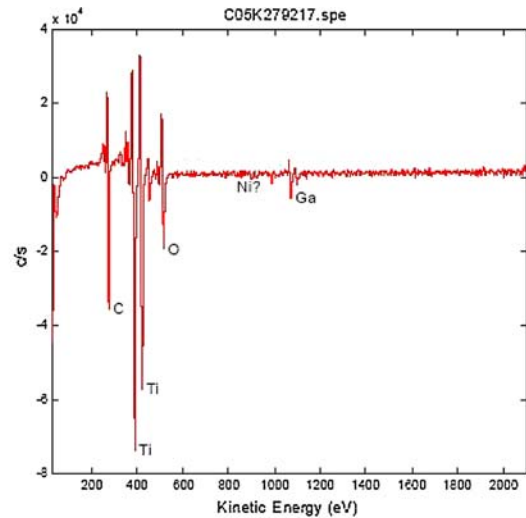
Fig. 3 (a) SEM image of carbide and oxides in specimen A3, and EDS line scans of (b) carbide, (c) isolated oxide (oxide-1), and (d) oxide in stringer (oxide-2)

Fig. 4 (a) An SEM image and (b) the corresponding AES spectrum of a Ti(C, O) carbide inclusion

carbides. In the analysis of A3 finished tube specimen, oxide inclusions were found as isolated particle as well as in elongated stringer. Figures 3(c) and (d) show the EDS line scans of an isolated oxide (oxide-1) and an oxide in a stringer (oxide-2), respectively. The results suggest that both oxides are identical in chemical composition that is rich in Ti and O but the Ni and C

contents are similar to those of the matrix. The lack of a noticeable difference in the C content between oxide and matrix suggests that the presence of C in the EDS spectrum of Fig. 5(c) must come from surface contamination. EDS mapping provides further verification on the elemental distribution within carbide and oxide inclusions as described above. Figure 6(a) displays an SEM micrograph of an A3 specimen containing both carbide and a fractured oxide. C, O, Ti, and Ni mapping in Fig. 6(b) confirms that the carbide contains higher levels of C, O, and Ti, but less Ni while the oxide is rich in O, Ti, and its C and Ni concentrations are comparable to those of the matrix.

A file in the International Centre for Diffraction Data (ICDD) suggests the O content in the oxide inclusion to be $Ti_4Ni_2O_{0.3}$ (Ref 10) but the stoichiometry would support the "Ti_4Ni_2O" atomic ratio. Since present analytical techniques are limited in providing quantitative data to resolve this issue, we continue to use the "$Ti_4Ni_2O_x$" nomenclature.

3.2 Effects of Melting and Tube Drawing Processes

As mentioned earlier, current supplies of NiTi materials exhibit noticeable lot-to-lot variations in inclusion size and distribution. For the sake of discussion, we present in Fig. 7 exemplary optical micrographs in the longitudinal view of 2.2 mm diameter tube specimens of A3, B, C, and D fabricated of VIM/VAR, VIM, standard VAR, and HP VAR materials, respectively, that we consider as typically representative. Two forms of inclusion morphology were observed; one of elongated stringer along the tube drawing direction and the other as isolated particles. The isolated inclusion count is quite high in VIM/VAR, VIM, and standard VAR materials, but appears to be reduced in HP VAR specimen. For the stringer type of inclusion, the tube specimen of VIM material (Fig. 7b), in general, has the lowest while the standard VAR material (Fig. 7c) has the highest stringer density.
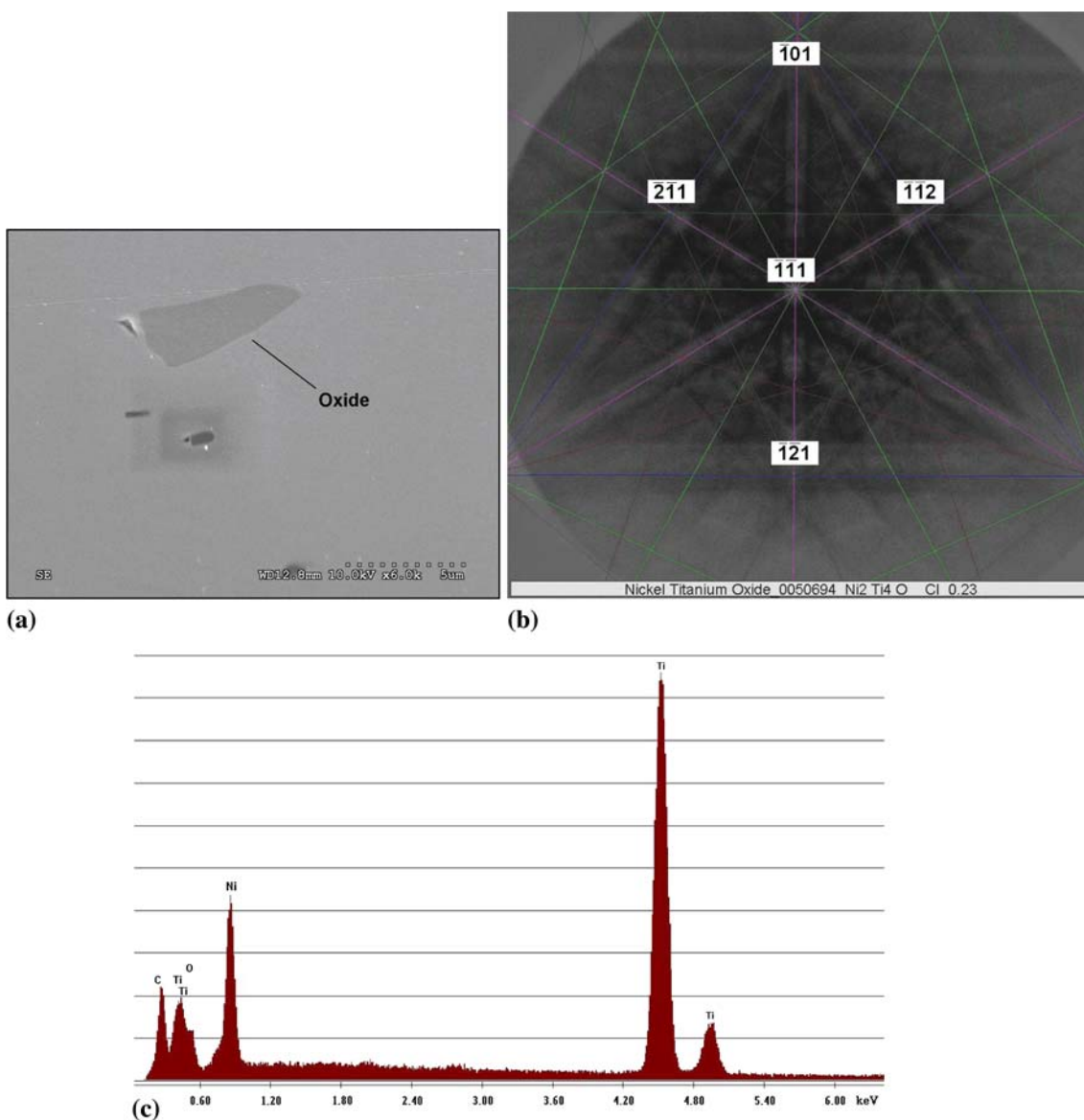
Fig. 5 (a) SEM image, (b) corresponding indexed EBSD pattern, and (c) EDS spectrum of an oxide-type inclusion in sample A1, which determined the most likely phase to be $Ti_4Ni_2O_x$ oxide
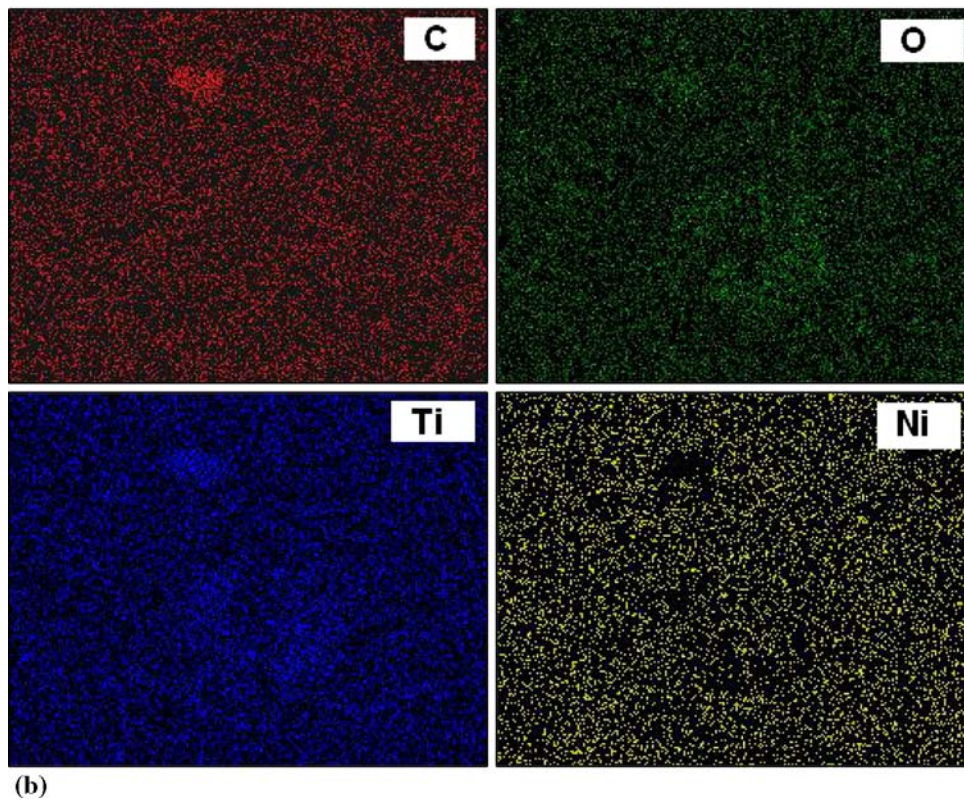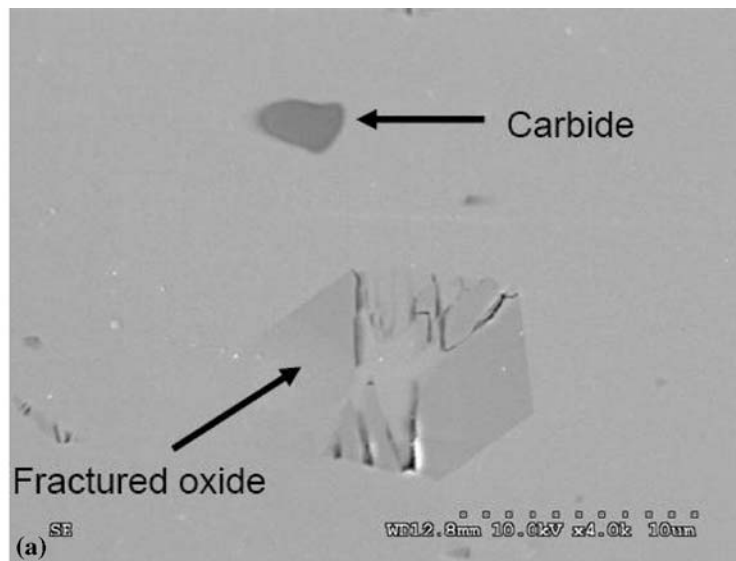
Fig. 6 EDS mapping of sample A3 showing the C, O, Ni, and Ti distribution in carbide and oxide inclusions
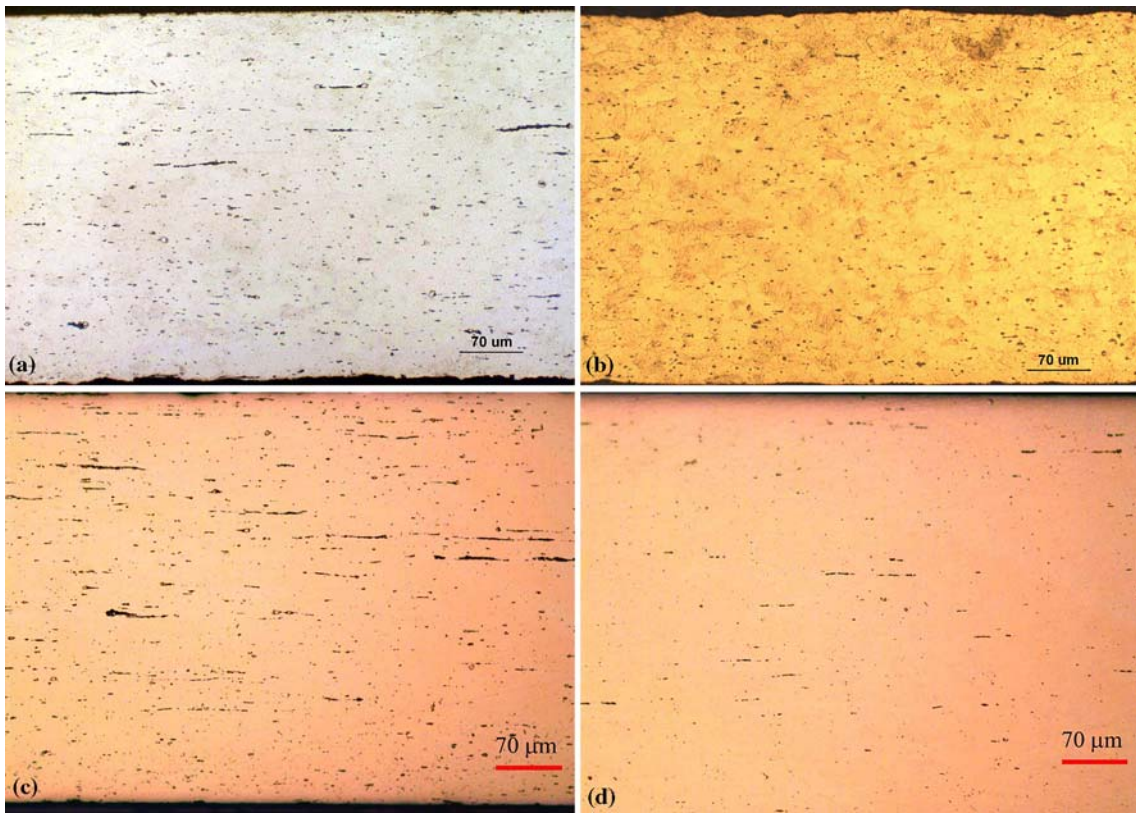
3.3 VIM/VAR Specimens

Regarding the type of inclusion in these materials of various melt processes, it is clear from Fig. 3 that both carbide and oxide are present in specimen A3, the tube of VIM/VAR material. The VIM/VAR material is therefore selected for studying the effect of inclusion chemistry on stringer formation. Light optical micrographs in Fig. 8 reveal the microstructure as the material goes through the tube drawing process from 31.0 mm diameter hot-rolled bar to 2.2 mm diameter tube. All inclusions in the starting hot-rolled bar (Fig. 8a) appear as isolated particles and no stringer was observed. In the micrograph of Fig. 8(a), carbides exhibit a rosy hue while the oxide has a similar contrast to the matrix. The color contrast presents a good way to differentiate carbides from oxide inclusions in optical metallography. Linear arrays of stringer along the drawing direction emerge at an intermediate size of 6.7 mm OD (Fig. 8b) and become more densely populated in the microstructure of the finished tube (Fig. 8c).

The SEM and EDS analyses on the stringers provided more detailed information about the effects of carbide and oxide on

Fig. 7 Exemplary optical micrographs of finished 2.2 mm diameter tube specimens: (a) A3 (VIM/VAR), (b) B (VIM), (c) C (standard VAR), and (d) D (HP VAR)
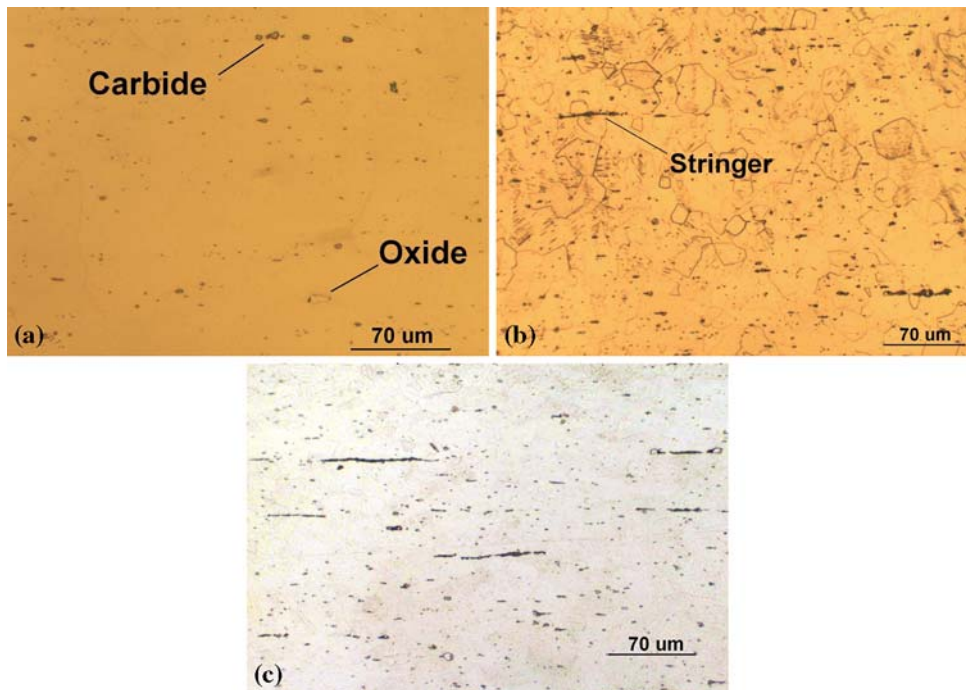
Fig. 8 Light optical micrographs of VIM/VAR specimens at various stages of tube drawing process: (a) A1 (31.0 mm OD hot rolled bar), (b) A2 (6.7 mm OD intermediate), and (c) A3 (2.2 mm finished tube)

their formation. The SEM micrographs in Fig. 9 display several examples of stringer morphology in specimen A3. The most frequently observed stringer is shown in Fig. 9(a) consisting of

broken oxide particles clustered in an elongated array along the tube drawing direction while carbides which are generally smaller than oxide in dimension usually remain as isolated

particles. Occasionally, fractured oxides not quite developed into stringers were observed (Fig. 9b). In some cases, particles of the carbide type were also found, preferentially in the area surrounding the end of the stringers (Fig. 9c). The observation of a number of A3 and other lots of tube specimens indicated that breaking-up of large oxides during cold drawing could be the most likely mechanism for stringers' formation, since in all cases the particles inside the stringers seemed to be small, fractured parts of a larger original particle (Fig. 9a-c). Occasionally, carbide particles were found to line up along the drawing direction forming a similar morphology to that of a stringer (Fig. 9d). But it is less apparent if the carbide particles inside this morphology evolved from breaking-up of a larger particle of carbide inclusion.

3.4 VIM Specimens

The majority of inclusion particles are small (less than 5 μm in diameter) and remained as isolated particles in tube specimen B as shown in the SEM micrograph of Fig. 10(a). The corresponding EDS line scan in Fig. 10(b) confirms that the inclusion is of the carbide type. No oxide inclusions were found in the specimen. Much less frequently than in the VIM/VAR material, stringers were found in the VIM tube specimen, an example of which is shown in the SEM micrograph of Fig. 11. Resembling the oxide stringer morphology in Fig. 9, a cluster

of small carbide particles are closely packed in an elongated array. Comparing the scale to that of a nearby isolated carbide particle, the string was likely developed from a large carbide particle (larger than 10 μm in diameter) which broke up during tube drawing.

3.5 VAR Specimens

Other than the lower inclusion density in the HP VAR material, the inclusion's type and morphology are fundamentally similar between the standard VAR (specimen C) and HP VAR (specimen D) tube specimens. All inclusions were found to be of the $Ti_4Ni_2O_x$ type as no Ti(C, O) type was observed. An SEM image and the corresponding line scan of an inclusion in specimen C are shown in Fig. 12 confirming the oxide chemistry. The morphology represents an example of small oxide particles, less than 2 μm in diameter, which were aligned along the drawing direction during tube drawing. A more typical stringer in specimen C is shown in the SEM micrograph of Fig. 13(a) where broken-up oxide particles are apparent. Oxide break-up can be more clearly seen in Fig. 13(b), an SEM micrograph showing fractured oxide inclusions before actually forming a stringer.

A typical example of oxide stringer in HP VAR tube specimen (specimen D) is exhibited in Fig. 14(a) where an enlarged SEM micrograph of the stringer is shown in
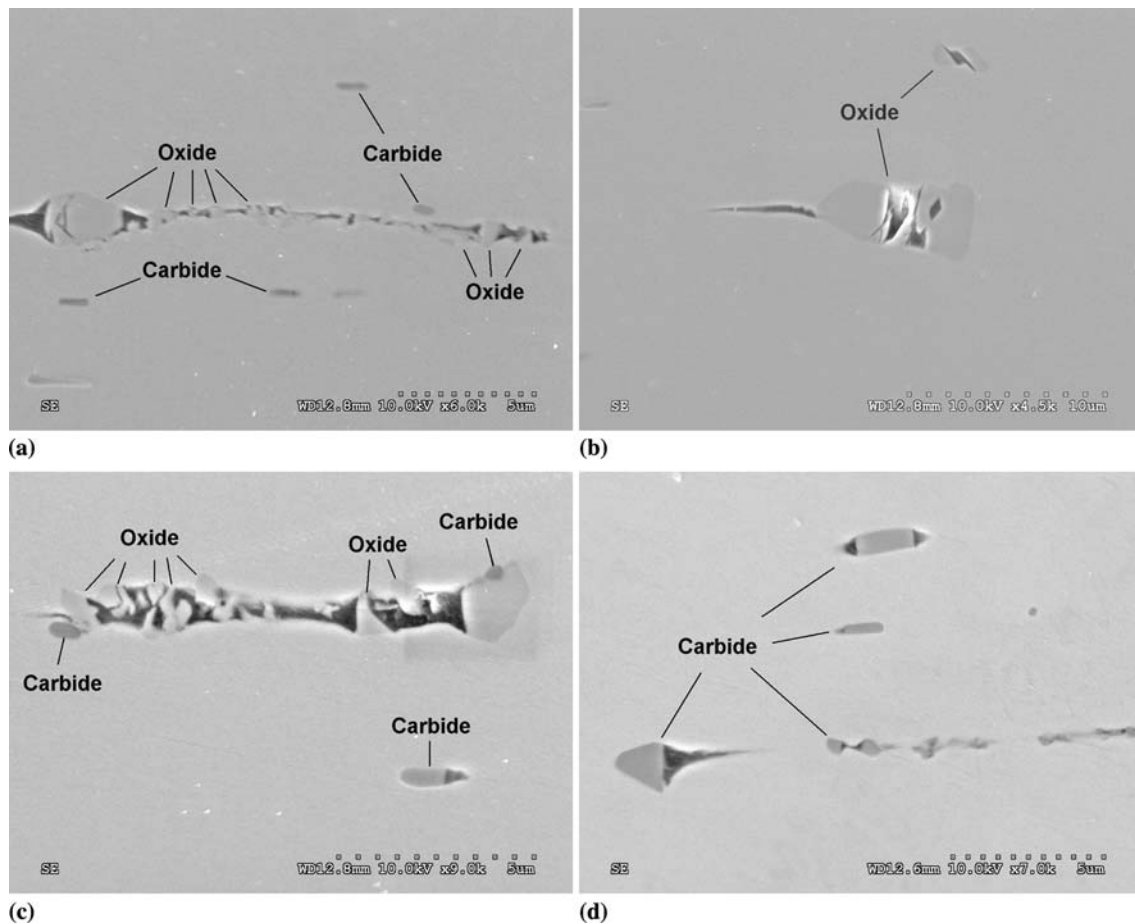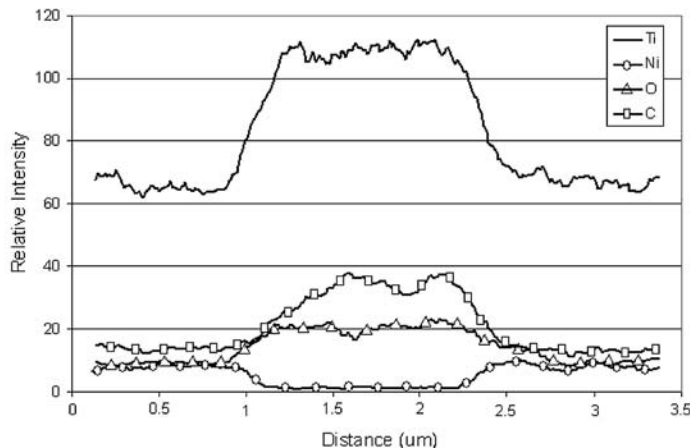

Fig. 9 SEM micrographs showing examples of stringer morphology in the 2.2 mm OD tube specimen A3
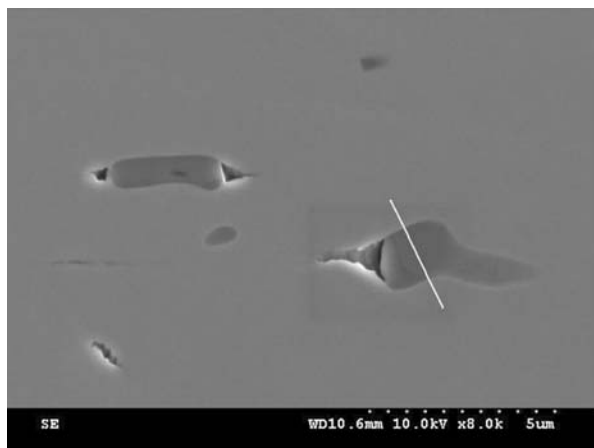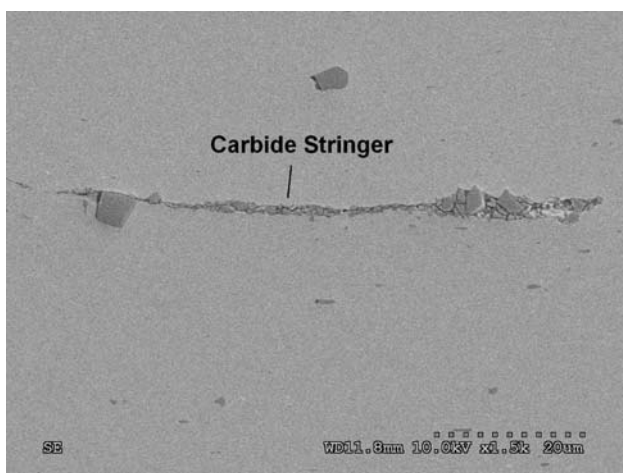
Fig. 10 (a) An SEM micrograph and (b) corresponding EDS line scan of Ti(C, O) carbide inclusion in specimen B


**Fig. 11** SEM micrograph of a carbide stringer in specimen B

Fig. 14(b). Both micrographs exhibit the same characteristics of fractured oxide particles as of the stringers in the standard VAR tube material (specimen C).

4. Conclusions

1. Combined use of SEM, EBSD, EDS, and AES demonstrated that oxygen is present in the carbide inclusion, hence the Ti(C, O) nomenclature, while the $Ti_4Ni_2O_x$ oxide inclusions have been shown to be rich in Ti and O relative to the matrix chemistry. However, present analyses are limited in providing quantitative data to determine the oxygen content in the oxide inclusion.

2. Both carbide and oxide inclusions are present in the VIM/VAR material. These inclusions appear as isolated particles in the hot-rolled bar but the oxide, generally larger in size than carbide, exhibits a greater propensity to
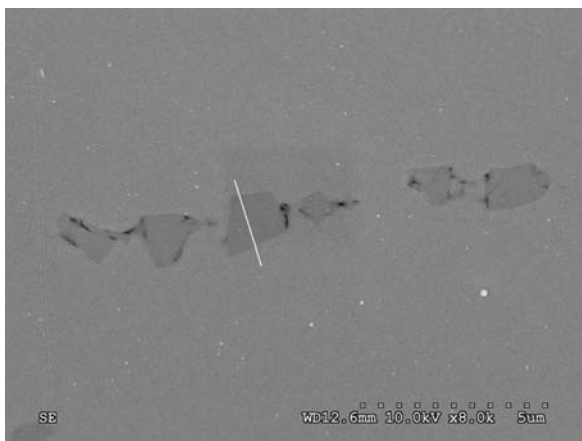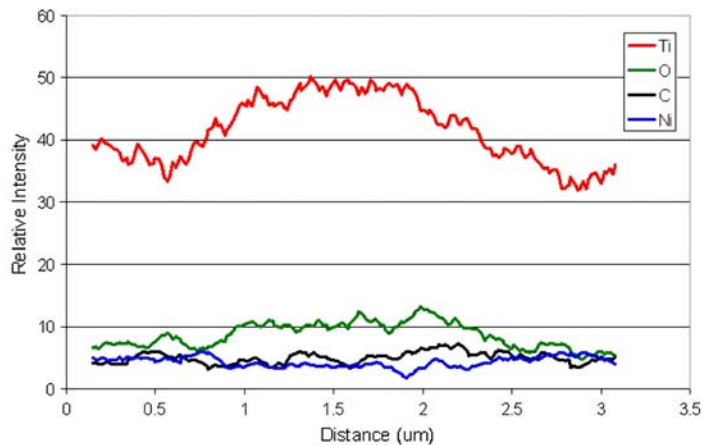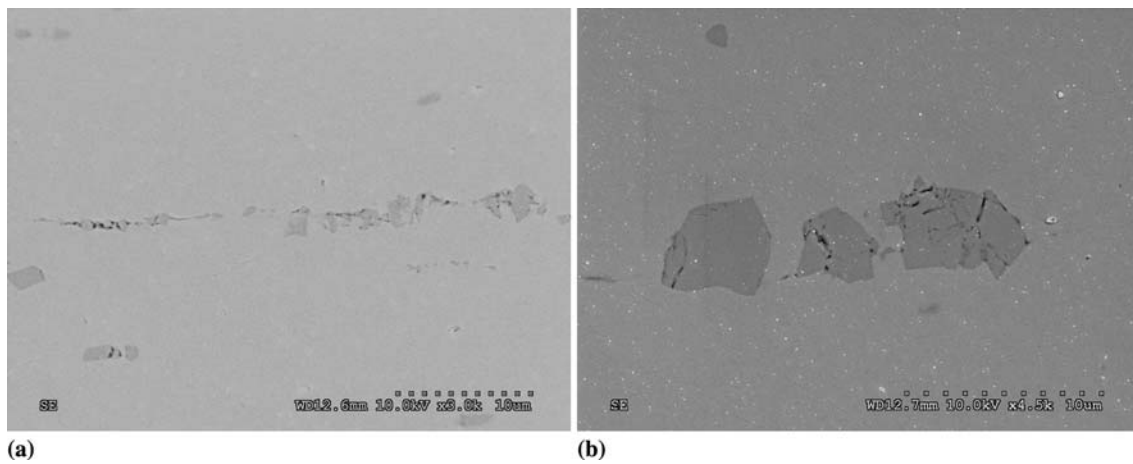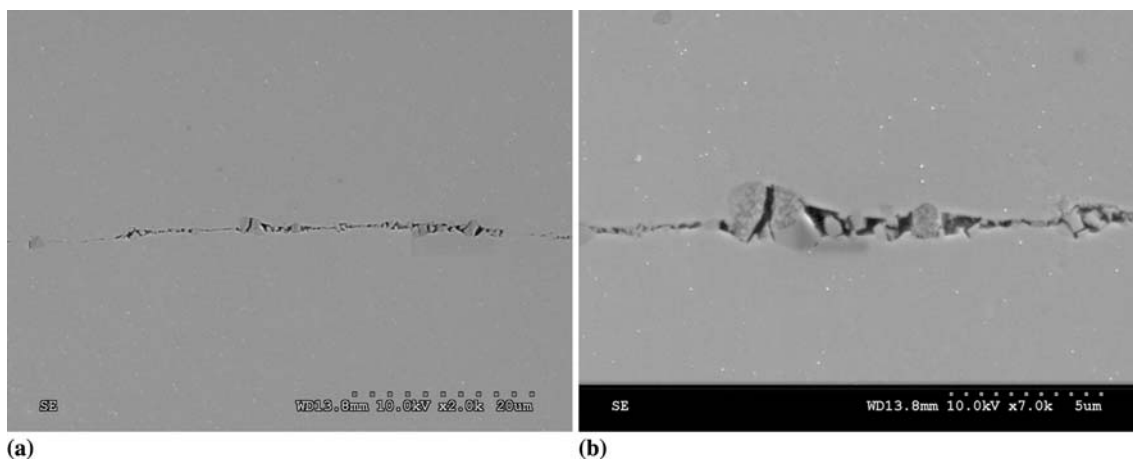

Fig. 12 (a) An SEM image of $Ti_4Ni_2O_x$ inclusions in the tube specimen of standard VAR material (specimen C) and (b) the corresponding EDS line scans

Fig. 13 SEM micrographs of (a) a typical oxide stringer and (b) an early stage of stringer formation showing partially broke-up oxide particles in standard VAR tube specimen C

Fig. 14 SEM micrographs of (a) a typical oxide stringer and (b) an enlarged area of (a) in HP VAR specimen D

fracture during tube drawing, breaking-up and forming elongated stringer along the drawing direction.

3. Inclusions in VIM material are essentially of the Ti(C, O) type and are generally small, less than 5 μm in diameter. The majority of these carbide inclusions remain as isolated particles during tube drawing, but occasionally, stringers of fractured carbide can develop from large carbide inclusions of greater than 10 μm in diameter.

4. Inclusions in both standard and HP VAR materials are of the $Ti_4Ni_2O_x$ type. While HP VAR material exhibits less inclusion and stringer densities than the standard VAR material, which has the highest stringer density among the specimens studied, the characteristics of stringers in both standard and HP VAR materials are fundamentally the same consisting of fractured oxide particles that broke-up during the tube drawing process.

References

1. S. Sabeti, M. Schillinger, J. Amighi, C. Sherif, W. Mlekusch, R. Ahmadi, and E. Minar, Primary Patency of Femoropopliteal Arteries Treated with Nitinol Versus Stainless Steel Self-Expanding Stents: Propensity Score-Adjusted Analysis, *Radiology*, 2004, **232**(2), p 516–521
2. D. Schneinert, S. Schneinert, J. Sax, C. Piorkowski, S. Bräunlich, M. Ulrich, G. Biamino, and A. Schmit, Prevalence and Clinical Impact of Stent Fractures After Femoropopliteal Stenting, *J. Am. Coll. Cardiol.*, 2005, **45**(2), p 312–315
3. M. Reinoehl, D. Bradley, R. Bouthot, and J. Proft, The Influence of Melt Practice on Final Fatigue Properties of Superelastic NiTi Wires, *Proceedings of The International Conference on Shape Memory and Superelastic Technologies*, S.M. Russell and A.R. Pelton, Eds., April 30–May 4, 2000 (Pacific Grove, CA), p 397–403
4. T. Habu, I. Kato, K. Mikajiri, and F. Yamashita, Study of Inclusion in Ni-Ti Alloys, *Proceedings of the International Conference on Shape Memory and Superelastic Technologies*, December 3–6, 2007 (Tsukuba, Japan), in press

5. S.M. Russell, Nitinol Melting and Fabrication, *Proceedings of the International Conference on Shape Memory and Superelastic Technologies*, S.M. Russell and A.R. Pelton, Eds., April 30–May 4, 2000 (Pacific Grove, CA), p 1–9

6. Standard Specification for Wrought Nickel-Titanium Shape Memory Alloys for Medical Devices and Surgical Implants, ASTM F2063-05, ASTM, 2005

7. Z. Zhang, J. Frenzel, C. Somsen, J. Pesicka, K. Neuking, and G. Eggler, Orientation Relationship Between TiC Carbides and B2 Phase in As-Cast and Heat Treated NiTi Shape Memory Alloys, *Mater. Sci. Eng. A*, 2006, **438–440**, p 879–882

8. R. Graham, B. Van Doren, R. Henson, and J. DiCello, Characteristics of High Purity Nitinol, *Proceedings of the International Conference on Shape Memory and Superelastic Technologies*, A.R. Pelton and T. Duerig, Eds., May 5–May 8, 2003 (Pacific Grove, CA), p 7–14

9. N. Morgan, A. Wick, J. DiCello, and R. Graham, Carbon and Oxygen Levels in Nitinol Alloys and the Implications for Medical Device Manufacture and Durability, *Proceedings of the International Conference on Shape Memory and Superelastic Technologies*, May 7–11, 2006 (Pacific Grove, CA), p 821–828

10. International Centre for Diffraction Data (www.icdd.com), Newtown Square, Pennsylvania, Release 2005